Numerical analysis of nonlinear interaction between a gas bubble and free surface in a viscous compressible liquid

Ji-Tuan Feng(冯集团),[1] Yun-Long Liu(刘云龙),[1, a)] Shi-Ping Wang(王诗平),[1] Shuai Zhang(张帅),[1, 2] and Longbin Tao(陶龙宾)[3]

[1)] *College of Shipbuilding Engineering, Harbin Engineering University, Harbin 150001, China*

[2)] *Nanhai Institute of Harbin Engineering University, Sanya 572024, China*

[3)] *Department of Naval Architecture, Ocean and Marine Engineering, University of Strathclyde, Glasgow G4 0LZ, United Kingdom*

Liquid viscosity has a potential effect on bubble dynamics. This paper is concerned with bubble dynamics in a compressible viscous liquid near the free surface. The liquid-gas flow is modeled using the Eulerian finite element method (EFEM) coupled with the volume of fluid method (VOF). The numerical results have been shown to be in excellent agreement with those from the spherical bubble theory and experiment. Parametric studies are carried out regarding the Reynolds number Re and the stand-off parameter γ_d. It clearly demonstrated that the liquid viscosity inhibits bubble pulsation, jet flow, free surface jet, and bubble splitting. Quantitatively, as Reynolds number Re decreases, the maximum bubble volume, jet tip velocity, free surface spike and crown height decrease, and the toroidal bubble splitting weakens. As the stand-off parameter γ_d increases, the maximum bubble volume, jet velocity, and bubble average pressure peak increase while the height of the free surface spike decreases. Close observation reveals that the free surface crown tends to disappear at small Re or large γ_d, further indicating the complex mechanism behind the crown spike evolution.

I. INTRODUCTION

Pulsating bubble dynamics have been widely applied in marine engineering, biomedicine and other fields, such as underwater explosion[1–8], ultrasonic bubble cleaning[9–13], microbubble ultrasound contrast agents[14–16], and digital printing technique[17–19]. When the initial bubble pressure is much greater than the pressure of the flow field, it will expand and start to oscillate under the action of the pressure gradient on both sides of the interface. At the same time, bubbles oscillating near the boundary (such as the free surface) can exhibit non-spherical dynamics such as jet generation due to the influence of asymmetric forces[20–27]. For the pulsating bubble near the free surface, the oscillation and migration of the bubble have strong nonlinear characteristics due to the influence of the deformation of the free surface[28–32]. If liquid viscosity is considered, the nonlinear characteristics of the bubble, such as jets and tears, will be changed, which will affect the application of the bubble in engineering. Thus it is necessary for us to study the interaction of pulsating bubbles and the free surface in viscous fluids.

Due to the common phenomenon of the pulsating bubble jet near the free surface in nature, many scholars have studied this phenomenon and found that depth, buoyancy, and pressure are the key factors affecting bubble dynamics and the free surface motion[33–47].Theoretical models such as the Rayleigh-Plesset equation[48], and the Keller-Miksis equation[49] can accurately predict the pulsating bubbles in free field, but they cannot include the influence of free surface and bubble migration. Recently, Zhang et al.[50] established a new oscillating bubble dynamics unified equation with an elegant mathematical form, considering various factors such as boundary, gravity, viscosity, compressibility, and bubble migration. This equation expands the applicability of bubble theory and provides a new idea for subsequent research. However, most of the theories are based on the assumption of spherical bubbles and cannot account for bubble jets and splitting, numerical and experimental methods are still widely used to study bubble dynamics. Blake and Gibson[33,34] observed the movement of bubbles adjacent to the free surface through the experiment of spark-generated bubbles. They found that the bubble is repelled during the collapse and generates downward liquid jets. Supponen[36] studied the bubble jet's generation conditions through many laser-induced bubble experiments and proposed an anisotropy parameter to describe the three states of the bubble jet, which can comprehensively consider the influence of the buoyancy of the bubble and the distance to the free surface. Zhang[37] used the discharge spark generator to study the interaction of the bubble and the free surface at different initial depths. Furthermore,

[a)] Corresponding author: yunlong_liu@hrbeu.edu.cn

they summarized the laws of bubble shapes and pulsation periods, heights of the water skirts and the free surface spikes, and jet tip velocities and identified six distinctive patterns of the free surface. Cerbus[42] observed the motion characteristics of the free surface jet and analyzed the formation mechanism of the second jet and the effect of the two control parameters. Unfortunately, the effect of liquid viscosity on the interaction between the pulsating bubble and the free surface has rarely been mentioned in previous experiments. For numerical techniques, the boundary element method (BEM) has been widely employed in studying non-spherical bubble dynamics because of low computational cost[51–55]. However, the traditional BEM was developed based on the potential flow theory, thus it is not easy to calculate the effect of the viscosity of the liquid on bubble dynamics. Based on the traditional BEM, Miksis[56] proposed Boundary Layer theory to deal with viscous bubble dynamics. Then Lunderen[57] and Boulton-Stone[58] extended the theory and obtained the continuous expression of normal and tangential components. Based on these studies, Li[54] used the Boundary Layer theory to study the effects of the Reynolds number on the movement of two bubbles close to the free surface and found that viscosity would depress the bubble movement. Lind[53] paid attention to the influence of viscoelasticity on bubble dynamics in the vicinity of the free surface. Moreover, Lind also found that viscoelasticity affected the bubbles' jet and changed the shape of collapsing bubbles. However, the boundary layer theory only calculates in a thin layer at the bubble boundary, which cannot accurately calculate the influence of viscous dissipation on the liquid outside the boundary layer. It is also challenging to consider the compressibility of the liquid at the same time.

Many numerical multiphase flow models based on domain methods are also widely used to analyze bubble dynamics, which can obtain complete flow data. Li[38] used the open-source software OpenFoam to numerically study the bubble bursting properties close to the free surface and found that gas flow plays an important role in the re-closure of burst bubbles. Singh[45] studied the internal gas dynamics of burst bubbles using the VOF method. Liu[39] combined FVM and FTM to investigate the dynamical characteristics of oscillating bubbles near the free surface at different depths and buoyancy. Saade[40] used the FVM solver to simulate the crown of bubble-induced generation, analyzed the influence of non-dimensional parameters such as Reynolds number and stand-off parameter on crown formation, and explained the mechanism of crown formation. Saade aimed to obtain stable free surface jets for application in the LIFT process, and therefore a lower initial pressure of the bubble was chosen. However, this is not suitable for simulating higher initial pressure bubbles such as underwater explosions and high-voltage spark bubbles. Bempedelis[41] numerically studied the dynamics of a bubble-free surface coupling system, focused on the dynamic characteristics and deformation of the free surface, and characterized the process of bubble-induced atomization. From the above analysis, previous researchers hardly consider the effects of liquid compressibility and viscosity simultaneously when analyzing the coupling effect between high-pressure bubbles and the free surface. However, compressibility and liquid viscosity have essential effects on the dynamic characteristics of high-pressure pulsating bubbles. For more accurate results, the compressibility effect should be considered[59]. The EFEM numerically solves the Navier-Stokes equation and fluid equation of state based on the domain approach. It can consider both the strong compressibility, viscosity, and pressure distribution of the fluid. The EFEM uses the operator splitting algorithm to separate the governing equations, which allows it to be flexibly combined with other numerical techniques to improve accuracy and applicability. At the same time, the combination of VOF for interface capture and reconstruction can accurately and flexibly simulate the splitting and merging process of two-phase interface deformation and topological relationship changes. This method can accurately simulate the complete stage of underwater explosion and the interaction between the bubble and the free surface.

The present paper establishes an axisymmetric dynamics model of the interaction between the free surface and bubbles using EFEM. The VOF is used to capture the fluid interface and study the effect of liquid viscosity on bubbles and free surface motion. The main contents are as follows: the second section describes the physical model, governing equations, and initial conditions of the problem, establish the bubble dynamics model, and verifies the accuracy of the numerical results. In section 3, the effects of liquid viscosity and distance on the bubble-free surface coupling dynamics are studied, and the mechanical mechanism is analyzed in detail. The fourth section draws some critical conclusions.

II. THEORETICAL AND NUMERICAL MODELS

A. Problem assumptions and governing equations

This study mainly focuses on the interaction between bubbles and the free surface. A sketch is shown in Fig.1(a) to describe the problem. An initial spherical bubble is placed in a static viscous liquid at a depth d below the free surface. The bubble can be induced by spark discharge, underwater explosion, or

air-gun, and the initial pressure is higher than the surrounding fluid. The bubble expands rapidly under pressure and interacts with the free surface. The non-reflection boundary condition is used for the edge of the computational domain[60]. An axisymmetric coordinate system is established as shown in Fig.1(a), where O, r, z, and φ represent the coordinate origin, radial coordinate, axial coordinate, and angular coordinate, respectively, and the computational domain size is $w \times h$. The gravity points to the negative direction of the z axis.

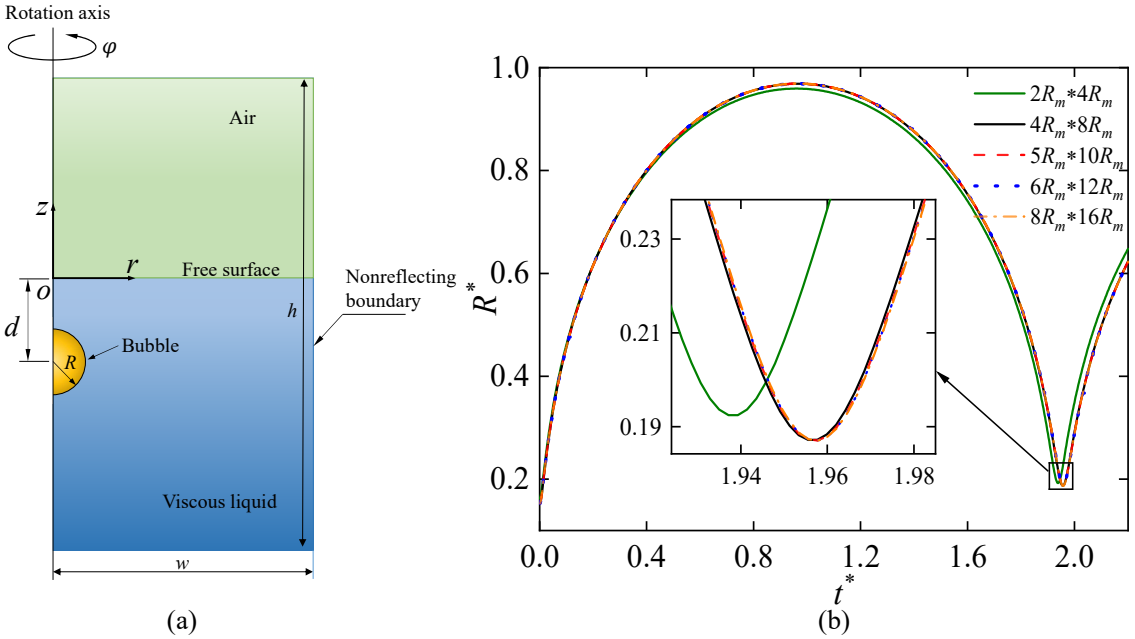

FIG. 1. (a)Configuration for the interaction between the single bubble and the free surface; (b)comparison of bubble radius in different calculation domain sizes $2R_m \times 4R_m$, $4R_m \times 8R_m$, $5R_m \times 10R_m$, $6R_m \times 12R_m$, and $8R_m \times 16R_m$.

In this paper, the effects of liquid viscosity on the interaction of a pulsating bubble and the nearby free surface were studied, while surface tension and heat conduction could be neglected[34,61–64]. In the current cylindrical coordinate system, the following governing equations can be established:

$$\begin{cases} \dfrac{\partial \alpha_i}{\partial t} + \nabla \cdot (\alpha_i \boldsymbol{v}) = \alpha_i \dfrac{\overline{K}}{K_i} \nabla \cdot \boldsymbol{v}, \\ \dfrac{\partial \alpha_i \rho_i}{\partial t} + \nabla \cdot (\alpha_i \rho_i \boldsymbol{v}) + \dfrac{\alpha_i \rho_i v_r}{r} = 0, \\ \dfrac{\partial \overline{\rho} \boldsymbol{v}}{\partial t} + \nabla \cdot (\overline{\rho} \boldsymbol{v} \otimes \boldsymbol{v}) + \dfrac{\overline{\rho} v_r \boldsymbol{v}}{r} + \nabla p = \overline{\rho} \mathbf{g} + \nabla \cdot \boldsymbol{\tau} + \dfrac{\boldsymbol{\tau}_r}{r}, \\ \dfrac{\partial \alpha_i \rho_i e_i}{\partial t} + \nabla \cdot (\alpha_i \rho_i e_i \boldsymbol{v}) + p \alpha_i \dfrac{\overline{K}}{K_i} (\nabla \cdot \boldsymbol{v} + \dfrac{v_r}{r}) + \dfrac{\alpha_i \rho_i e_i v_r}{r} = \Phi_i, \end{cases} \tag{1}$$

which represent the volume fraction, mass conservation, momentum conservation in r and z directions, and energy conservation equations, respectively. Here, the subscript 'i' represents the type of fluid, α represents volume fraction which is the volume ratio of the fluid phase to the element and $\sum \alpha_i = 1$, ρ is the density of the fluid and $\overline{\rho} = \alpha_1 \rho_1 + \alpha_2 \rho_2$ is the average density, $K = \rho c^2$ is fluid bulk modulus, c is the sound speed of the fluid, p is the pressure, and e is the specific internal energy of the fluid, $\boldsymbol{v} = (v_r, v_z)^T$ is the velocity vector of the fluid, $\mathbf{g}$ is gravity vector. The subscripts r, z indicate the components of the vector in the r and z directions, respectively. $\boldsymbol{\tau}$ is the viscous stress tensor, and $\boldsymbol{\tau}_r = (\tau_{rr} - \tau_{\varphi\varphi}, \tau_{rz})^T$ is a component of tensor $\boldsymbol{\tau}$. The symbol '$\otimes$' is the tensor product operator, and $\nabla = (\frac{\partial}{\partial r}, \frac{\partial}{\partial z})$ is the gradient operator. Besides, in the mixing element, the average bulk modulus $\overline{K}$ can be determined by

$$\overline{K} = \frac{K_1 K_2}{\alpha_1 K_2 + \alpha_2 K_1}. \tag{2}$$

In a Newtonian fluid, the viscous stress tensor $\boldsymbol{\tau}$ can be expressed as[38]

$$\begin{cases} \boldsymbol{\tau} = \Sigma\alpha_i\boldsymbol{\tau}_i = \Sigma\alpha_i\mu_i\left[\nabla\boldsymbol{v} + \nabla\boldsymbol{v}^T - \frac{2}{3}\left(\nabla\cdot\boldsymbol{v} + \frac{v_r}{r}\right)\mathbf{I}\right], \\ \tau_{\varphi\varphi} = \Sigma\alpha_i\mu_i\left[2\frac{v_r}{r} - \frac{2}{3}\left(\nabla\cdot\boldsymbol{v} + \frac{v_r}{r}\right)\right], \end{cases} \tag{3}$$

where μ is the dynamic viscosity coefficient, and $\mathbf{I}$ is the unit matrix. For the energy conservation equation,

$$\Phi_i = \boldsymbol{\tau}_i : \nabla\boldsymbol{v} = \tau_{rr\_i}\frac{\partial v_r}{\partial r} + \tau_{rz\_i}\frac{\partial v_r}{\partial z} + \tau_{zr\_i}\frac{\partial v_z}{\partial r} + \tau_{zz\_i}\frac{\partial v_z}{\partial z} + \tau_{\varphi\varphi\_i}\frac{v_r}{r}, \tag{4}$$

which represents the viscous dissipation energy. The equation of state(Eos) of the fluid is used to close the governing equations of the compressible fluid. In present work, the Tammann equation[65] is used to describe the fluid state:

$$p = \rho e(\zeta - 1) - \zeta P_w. \tag{5}$$

In this paper, the initial density ρ of liquid and gas is 1000.0 kg/m^3 and 1.29 kg/m^3, respectively. ζ is the specific heat ratio of fluid, which is 7.15 and 1.25 for liquid and gas, respectively. P_w = 3.309e8 Pa is the pressure constant of water. For gas, $P_w = 0$ Pa is chosen to represent the ideal gas.

B. Eulerian Finite Element Method(EFEM)

The EFEM has been maturely applied and has obtained reliable results in solving underwater explosion bubble dynamics[66–69]. The operator split technique is the key to EFEM, and the previous literature[60,62,66,70,71] has described the operator split method in detail. The operator split method separates the convection term from the governing equation to divide the equation into two parts for calculation, called the Lagrangian phase and the Eulerian phase. The explicit finite element method calculates the equation without the convection term in the Lagrangian phase. Thus, the fluid material follows the mesh movement in a single time increment. The convection term in the equation is calculated in the Eulerian phase, where the fluid remains stationary, the mesh returns to its original position, and material transport occurs between adjacent elements. A two-step calculation is performed in a time increment to move the fluid material while the mesh remains stationary. The equation solved in the Lagrangian phase does not contain a convection term and can be solved by the FEM. Combining the mass conservation equation and Gauss formula, the following momentum integral form can be obtained:

$$\iint_\Omega \overline{\rho}\frac{\partial\boldsymbol{v}}{\partial t}\phi\mathrm{d}s = \iint_\Omega \left(p\nabla\phi + \overline{\rho}\mathbf{g}\phi - \boldsymbol{\tau}\cdot\nabla\phi + \frac{\boldsymbol{\tau}_r}{r}\phi\right)\mathrm{d}s - \int_{\partial\Omega} p\phi\boldsymbol{n}\mathrm{d}l + \int_{\partial\Omega}\boldsymbol{\tau}\phi\cdot\boldsymbol{n}\mathrm{d}l, \tag{6}$$

where $\partial\Omega$ is the outer boundary of the element volume Ω, ϕ is a weight function determined by the element shape, and $\boldsymbol{n} = (n_r, n_z)$ is the interface unit normal vector. The variables on the right-hand side of Eq.(6) are known, and the element nodal acceleration can be calculated according to Newton's second law of motion:

$$\mathbf{M}\mathbf{A}_{\mathrm{node}} = \mathbf{F}_{\mathrm{node}}, \tag{7}$$

where $\mathbf{M} = \iint_\Omega \overline{\rho}\phi\mathrm{d}s$ is the nodal mass matrix, $\mathbf{A}_{\mathrm{node}}$ is the nodal acceleration vector, and $\mathbf{F}_{\mathrm{node}}$ is the nodal force, which can be calculated from the right-hand side of Eq.(6). From this, the nodal velocity and displacement can be calculated by the explicit finite element method, and Tang[67] gave the calculation formula for any node:

$$\boldsymbol{v}^{k+1/2} = \boldsymbol{v}^{k-1/2} + \boldsymbol{a}^k\Delta t, \tag{8}$$

$$\boldsymbol{x}^{k+1} = \boldsymbol{x}^k + \boldsymbol{v}^{k+1/2}\Delta t, \tag{9}$$

where Δt is the time increment, k is the time count, $\boldsymbol{a}$ is the nodal acceleration vector obtained from Eq.(7). Therefore a new node position is obtained, where the mesh and the fluid material move together, and the material inside the element at the current stage has not changed. However, the expansion and contraction

of the element cause change in the material's physical properties. The changes in volume, mass, and energy are calculated according to the continuity equation and energy equation after operator splitting:

$$\begin{cases} \dfrac{\partial \alpha_i}{\partial t} = -\alpha_i \nabla \cdot \boldsymbol{v} + \alpha_i \dfrac{\overline{K}}{K_i} \nabla \cdot \boldsymbol{v}, \\ \dfrac{\partial \alpha_i \rho_i}{\partial t} = -\alpha_i \rho_i \nabla \cdot \boldsymbol{v} - \dfrac{\alpha_i \rho_i v_r}{r}, \\ \dfrac{\partial \alpha_i \rho_i e_i}{\partial t} = \Phi_i - \left(\alpha_i \rho_i e_i + p \alpha_i \dfrac{\overline{K}}{K_i} \right) (\nabla \cdot \boldsymbol{v} + \dfrac{v_r}{r}). \end{cases} \tag{10}$$

At this point, the calculation of the Lagrangian phase is completed, and the fluid deforms with the mesh.

In the Eulerian phase, the material is fixed, and the mesh returns to its original position. During this process, volume transport occurs between adjacent elements. The convection volume can be obtained by integrating over the edges of the mesh. For single-phase elements, the fluid transport volume equals the mesh convection volume. However, for multiphase elements, the fluid transport volume on each mesh edge needs to be determined based on the location of the fluid interface within the element. In this paper, the second-order algorithm Piecewise Line Interface Calculation(PLIC) is applied to construct a linear fluid interface[72], and the fluid's transport of various variables is calculated by combining it with Monotone Upwind Schemes for Conservation Laws (MUSCL)[73]. The Eulerian phase of EFEM is described in detail by Tian[66,72], and these numerical techniques will not be repeated again. After the Eulerian phase, the element's mass, momentum, and energy are updated. After the material has been transported, the fluid pressure p needs to be updated using Eq.5. At this point, we have completed the calculation of a time increment.

This model must satisfy the CFL condition to ensure numerical stability. Therefore, the time increment Δt is limited by

$$\Delta t = C_o \left(\frac{l}{|\boldsymbol{v}_{max}| + c} \right)^{min}, \tag{11}$$

where l is the characteristic size of the mesh, and the superscript min indicates the minimum value of all elements. The Courant number $C_o = 0.3$ is chosen in this paper. The sound speed c can be expressed as[66]

$$c^2 = \frac{\zeta (p + P_w)}{\rho}, \tag{12}$$

when the Tammann equation is given.

C. Initial conditions and dimensionless parameters

Fig.1(a) illustrates the calculation model in this paper. At the initial moment, the bubble is located in a static viscous liquid, the depth from the free surface is d, the initial bubble radius is R_0, and the bubble pressure is P_0, respectively. The atmospheric pressure of the air above the free surface is $\mathrm{P_{atm}}$=101 kPa.

In order to avoid introducing errors due to different units or the numerical accuracy of the computer in the study of the same problem, dimensionless variables are used to simulate bubble dynamics. The expected maximum radius R_m of the spherical pulsation of the bubble in the inviscid and incompressible free field is used as the length scale. Moreover, the initial density of the viscous liquid is used as the density scale $\rho_{ref} = \rho_l$, and the ambient pressure $P_{ref} = \mathrm{P_{atm}} + |\mathbf{g}| d \rho_{ref}$ is used as the pressure scale. Therefore, the scales of velocity, time, and acceleration can be represented separately, as shown in Table I. According to these dimensionless scales, the case parameters of bubbles can be dimensionless in Table II. In this paper, the buoyancy parameter δ represents the gravity effect, the strength parameter ε represents the initial pressure, the stand-off parameter γ_d represents the dimensionless inception depth, the Mach number Ma represents the compressibility of the liquid (c_∞ is the sound speed in the liquid at infinity), and the Reynolds number Re represents the viscosity effect. The dimensionless radius and time are denoted as $R^* = R/R_m$ and $t^* = t/[R_m(\rho_{ref}/\mathrm{P}_{ref})^{1/2}]$ respectively, and other variables are expressed in the same way, in which the superscript '$*$' represents dimensionless. Unless otherwise specified, all subsequent analyses are performed using dimensionless variables.

TABLE I. Basic variables for dimensionless scales.

Velocity(V_{ref})	Time(T_{ref})	Acceleration(A_{ref})
$\sqrt{\frac{P_{ref}}{\rho_{ref}}}$	$R_m\sqrt{\frac{\rho_{ref}}{P_{ref}}}$	$\frac{P_{ref}}{R_m\rho_{ref}}$

TABLE II. Critical dimensionless case parameters.

δ^2	ε	γ_d	Ma	Re
$\frac{\rho_{ref}\lvert\mathbf{g}\rvert R_m}{P_{ref}}$	$\frac{P_0}{P_{ref}}$	$\frac{d}{R_m}$	$\frac{\sqrt{P_{ref}/\rho_{ref}}}{c_\infty}$	$\frac{R_m\sqrt{\rho_{ref}P_{ref}}}{\mu}$

D. Validation and convergence test

Before starting the verification, we first analyze the convergence of the computational domain. The computational domain sizes of $2R_m \times 4R_m$, $4R_m \times 8R_m$, $5R_m \times 10R_m$, $6R_m \times 12R_m$, and $8R_m \times 16R_m$ are selected for numerical simulation. The radius time history is shown in Fig.1(b), from which it can be found that the results are approximately the same except for $2R_m \times 4R_m$, indicating that the current calculation results are plausible. Although the difference in the radius curves in Fig.1(b) is not particularly obvious, in our numerical results, the bubble shape appears nonphysically distorted in the $2R_m \times 4R_m$, which indicates that the boundary affects the bubble in a smaller computational domain. To avoid the error caused by the free surface jet impacting the boundary of the computational domain, we select $6R_m \times 12R_m$ for calculation. Then we compare the model with theoretical and experimental results to verify the accuracy of the bubble dynamics model. First, we affirm the validity of the viscosity in our numerical model. The unified equation for bubble dynamics proposed by Zhang[50] can be used to describe bubble pulsation and migration in the free field of a viscous fluid. Taking a single spherical pulsating bubble in an infinite domain as the research object and ignoring the influence of initial velocity and surface tension, the bubble pulsation equation and migration equation of the simplified unified equation can be expressed as:

$$\left(\frac{c-\dot{R}}{R}+\frac{\mathrm{d}}{\mathrm{d}t}\right)\left[\frac{R^2}{c}\left(\frac{1}{2}\dot{R}^2+\frac{1}{4}\boldsymbol{v}_m^2+\frac{P_b-P_a}{\rho}\right)\right]=2R\dot{R}^2+R^2\ddot{R}, \tag{13}$$

$$C_a(R\dot{\boldsymbol{v}}_m+3\dot{R}\boldsymbol{v}_m)-\mathbf{g}R+\frac{3}{8}C_d\xi\left(\boldsymbol{v}_m\right)=0, \tag{14}$$

where R is the bubble radius, c is the sound speed of the external fluid, P_a is the ambient pressure at the bubble center, $P_b = P_{gas} - 4\mu\dot{R}/R$ is the fluid pressure on the outer bubble surface, P_{gas} is the internal bubble pressure, C_a is the added mass coefficient, C_d is the drag coefficient, $\boldsymbol{v}_m$ is the migration velocity, $\xi(\cdot) = (\cdot)|\cdot|$ is a signed square operator, and the top dot represents the first or second derivatives of the variable for time. When the migration of bubbles is not considered, Eq.13 can be further degenerated to the Keller-Miksis[49] equation. The KM(Keller-Miksis) equation improves the RP equation and includes the effect of fluid compressibility. Therefore, the KM equation is also used to compare the results of this paper.

Select the strength parameter $\varepsilon = 100$(which is considered a reasonable value[74]), the buoyancy parameter $\delta \approx 0.1$, the gravity acceleration $|\mathbf{g}| = 9.8$ m/s^2, the speed of sound $c = 1536$ m/s(according to Eq.12), the added mass coefficient $C_a = 1.0$, the drag coefficient $C_d = 0.5$, and ignore the surface tension, assume that the maximum dimensionless bubble radius is 1.0 in incompressible and inviscid cases. According to the relationship between the bubble radius and initial bubble pressure given by Klaseboer[2], the dimensionless initial radius R_0^*=0.149 is obtained. The numerical results are compared with Zhang et al.[50] and the KM equations at Re=100 as shown in Fig.2, where Re=∞ represents the inviscid case. The bubble migration distance of KM equation is zero because gravity is not considered. It can be found that the maximum bubble radius decreases significantly when Re=100. Due to the liquid compressibility effect, the bubble does not reach the expected maximum radius R_m. However, the bubble radius evolution and migration curves of numerical simulation are in good agreement with the theoretical model, indicating that the EFEM bubble dynamics model can accurately predict the effect of viscosity on bubble motion.

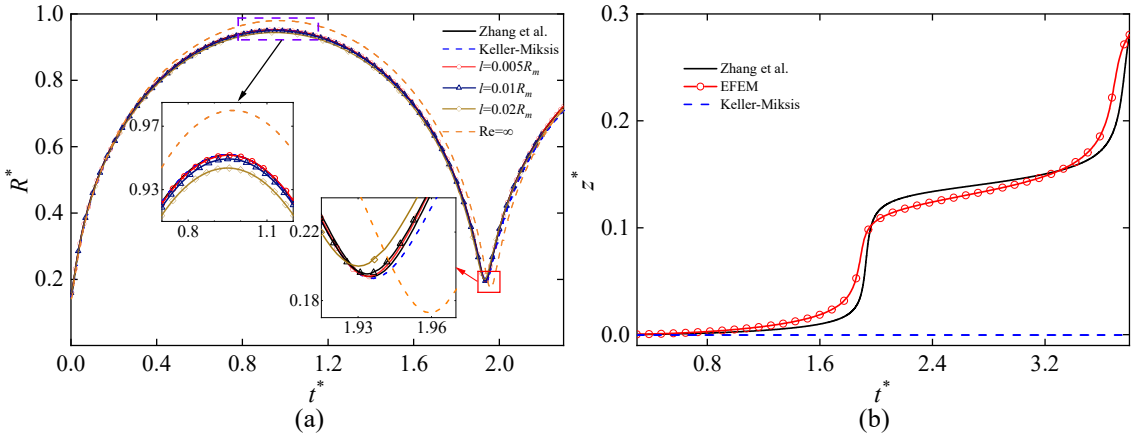

FIG. 2. Comparison of bubble radius evolution(a) and bubble migration(b) between EFEM and theoretical model at Re=100; (a)convergence analysis of equivalent radius for different mesh sizes $l = 0.005R_m$, $l = 0.01R_m$, and $l = 0.02R_m$.

In order to eliminate the influence of the mesh size on the model calculation results, it is necessary to carry out the convergence analysis. Set the calculation mesh size to $0.005R_m$, $0.01R_m$, and $0.02R_m$, respectively. The evolution of bubble radius with time is shown in Fig.2(a). As the mesh size decreases, the bubble radius curve converges to a theoretical solution. In order to take into account the calculation efficiency, the grid size is selected as $l = 0.01R_m$ in this paper. In addition, the numerical model is compared with the spark discharge experiment in glycerol. The experiment was carried out in a cube tank with a side length of 300mm and a glycerol depth of 200 mm. The density of glycerol ρ=1261 kg/m^3 and the dynamic viscosity μ=1499 mPa $\cdot$ s (20°C), respectively. Bubbles were generated by spark discharge using a high voltage device of 1800 V. The motion of bubbles and the free surface was captured by a high speed camera(Phantom V711). In the numerical model, a bubble with an initial radius of 4.1 mm is placed 26.1 mm below the free surface, and the initial pressure is set to $100P_\infty$ (P_∞ represents the liquid pressure at infinity at the same depth as the bubble). According to Zhang et al.[50], the expected maximum radius of the bubble was R_m=27.5 mm, thus the dimensionless inception depth was $\gamma_d = 0.95$, and the Reynolds number Re=183. The interaction of the bubble with the free surface is simulated using the EFEM model.

The main results are shown in Fig.3(a). The numerical results show the changes in the fluid pressure (contour map) and the bubble boundary (black line). At $t = 2.6$ ms, the bubble reaches a radius of 26.67 mm, lower than the expected maximum bubble radius(27.5mm), mainly caused by the liquid viscosity and the free surface effect. The kinetic viscosity of glycerol is strongly dependent on temperature. Spark discharge causes a change in the temperature of the surrounding fluid temperature, which leads to a change in viscosity. Unevenly distributed fluid viscosity can lead to errors between numerical and experimental results. There is a slight difference in the period caused by complicated reasons. First, the initial bubble formed by the spark discharge has complex dynamical properties rather than a spherical static bubble. Second, the gas inside the bubble in the experiment is water vapor rather than ideal gas. In addition, Unevenly distributed fluid viscosity affects the motion of the bubble. The bubble and the free surface shapes calculated by the numerical model agree with the experiments, indicating that this paper's model can simulate the motion of bubbles and the free surface in viscous fluids. The bottom of Fig.3(b) also compares the interfaces with viscous (Re=183) and non-viscous (Re=∞) fluids in the same case. It can be found that the liquid viscosity hinders the rise of the free surface, while the effect on the bubble position is not significant. This is because the free surface jet velocity is much smaller than the bubble expansion velocity. The free surface has a smaller local Reynolds number, resulting in a more significant viscous effect. The effect of viscosity on the bubble is mainly reflected in the bubble jet and shape. For example, in the fourth subfigure of 3(b), bubbles split in a viscosity-free liquid but not in a viscous liquid. It indicates that viscosity has an essential effect on the bubble-free surface coupled system.

The above results show that the EFEM bubble dynamics model can accurately simulate the interaction of bubbles and the free surface in compressible viscous fluids. This paper will use this model to study the effects of different parameters.

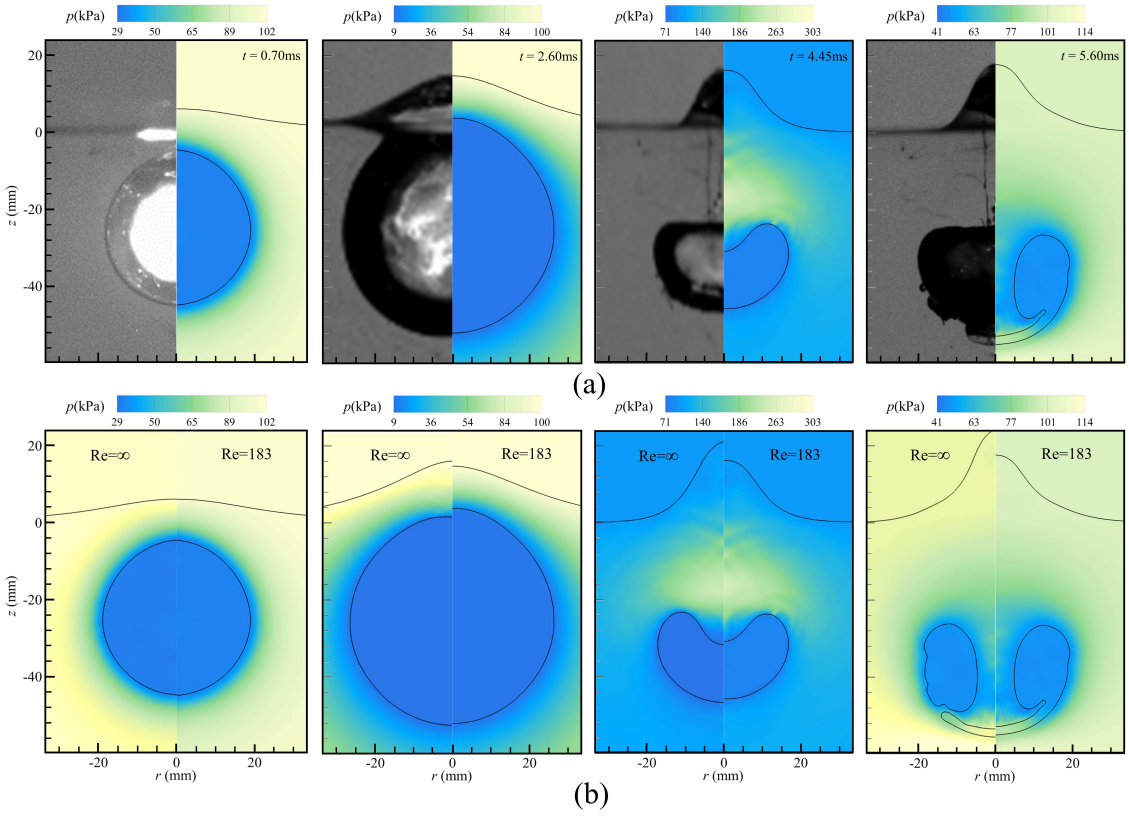

FIG. 3. (a)Comparison of EFEM bubble dynamics model(right) with experimental results(left) in glycerol at t=0.70ms, 2.60ms, 4.45ms, 5.60ms; (b)comparison of results for viscous(right) and non-viscous(left) fluids. The black line represents the bubble boundary and the free surface boundary; the colored contour represents the pressure field.

III. RESULTS AND DISCUSSION

Scholars have extensively studied the dynamics of bubbles in non-viscous fluids. However, when small bubbles are moving in highly viscous liquids, the effect of viscosity on bubble dynamics must be considered, which has potential value in the fields of the food-chemical industry. This section will discuss the bubble and the free surface coupling system's dynamic characteristics at different viscosity and depths. In the real problem, the influence of surface tension is feeble. In order to study only the effect of viscosity, the bubble surface tension effect is not considered. Therefore, our numerical results are not applicable to the bubble dynamics problem with dominant surface tension. In addition, due to the small Reynolds number, it is not necessary to solve the turbulence problem in this paper. The maximum bubble radius $R_m = 0.02$m and the dimensionless initial radius $R_0^* = 0.149$ were selected in the simulation. In order to avoid boundary effects, the computational domain is set to $6R_m \times 12R_m$, and other dimensionless parameters are $\varepsilon = 100$ and $\delta = 0.044$, respectively. The initial dimensionless depth and Reynolds number are determined according to the cases, and the grid size $l = 0.01R_m$ was used for simulation.

A. Bubble dynamics with different viscosity

In order to analyze the viscous effects, the computations are carried out for $\mathrm{Re} = 50, 100, 200, 400, \infty$ and $\gamma_d = 0.5$, where $\mathrm{Re} = \infty$ for the inviscid case. Fig.4 shows the evolution results of bubbles and the free surface for $\mathrm{Re} = \infty$, 100, and 50, respectively.

In Fig.4, (a)-(d) display the bubbles at the maximum volume, the jet penetration, the minimum volume, and the second maximum volume. Under initial high pressure, the bubble expands rapidly and radiates pressure waves outwards. Due to the influence of the free surface and gravity, the bubble expands faster upwards. Meanwhile, the free surface bulges under the push of the bubble. Fig.4(a) shows that when the

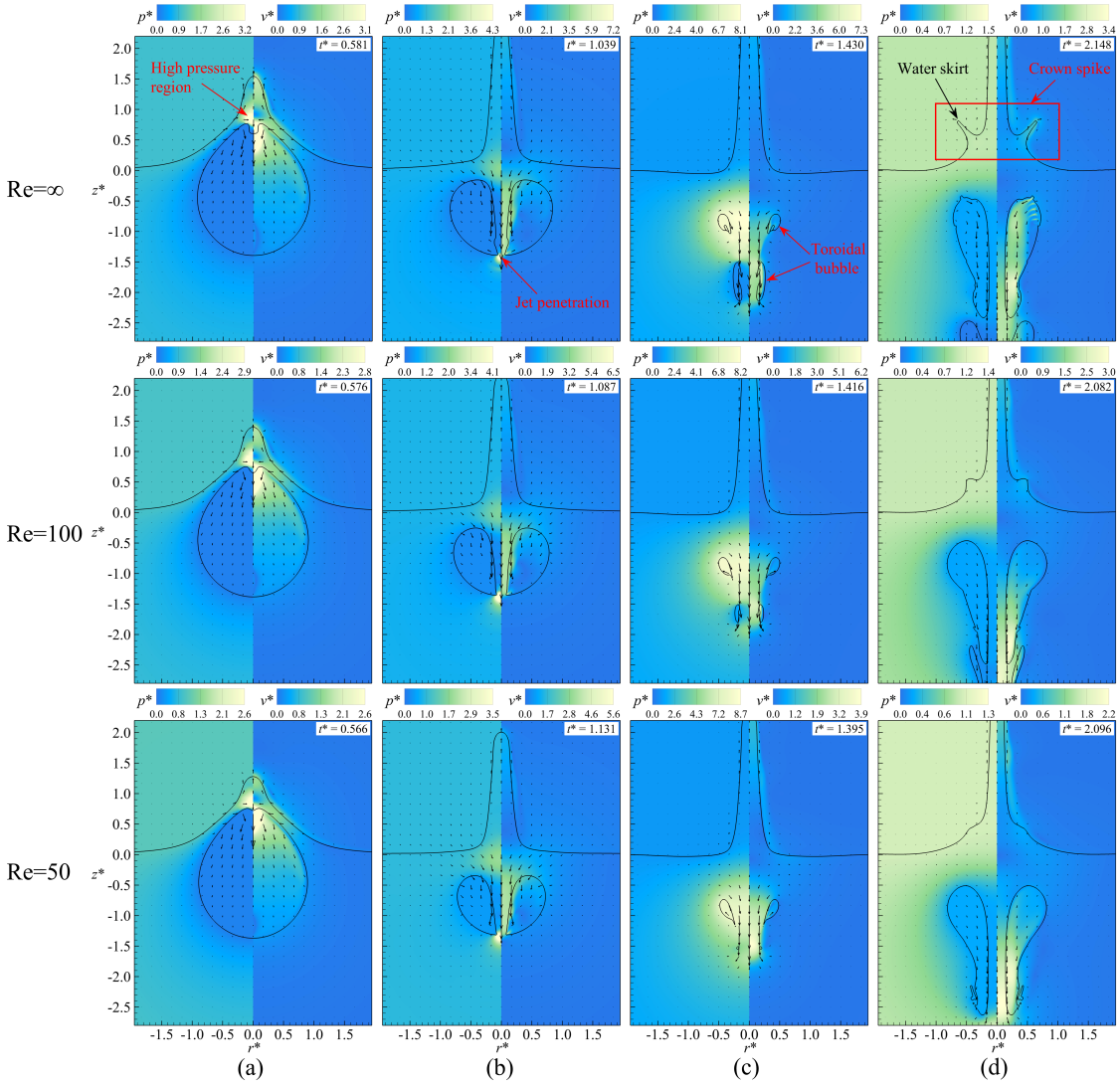

FIG. 4. Re $= \infty, 100, 50$, $\gamma_d = 0.5$ bubbles at four important moments of pressure and velocity contours: (a) maximum volume; (b) jet penetration; (c) minimum volume; (d) maximum volume in the second cycle of pulsation. The black line represents the bubble boundary and the free surface boundary; the left colored contour represents the pressure field; the arrow and the right colored contour represent the velocity field.

bubble reaches maximum radius, the liquid on both sides flows towards the top of the bubble and generates a high-pressure region. Due to the high-pressure region, the top interface collapses faster, forming a jet that points to the inside and pushes the free surface to move upward rapidly to form a sharp jet. Under the continuous action of pressure, the top jet of the bottom forms a toroidal bubble, and this impact will create a high-pressure region, as shown in Fig.4(b). Due to the small stand-off parameter γ_d, the bubble has not yet collapsed the minimum volume when the jet penetrates. The bubble continues to shrink and generate an annular "sideways jet" on the side wall pointing to the inside of the bubble, which will cause the bubble to split into two smaller toroidal bubbles, as shown in Fig.4(c), called toroidal bubble splitting. After the bubble collapses to the minimum volume, the internal pressure is greater than the external pressure, and the bubble begins to expand again into the second pulsation period. With the pulsation of the toroidal bubble, a low water skirt is formed around the free surface, also called a crown spike because of its shape resembling a crown. The formation mechanism of the crown is complex. Youssef[40] pointed out that crown is caused by the combined action of flow focusing induced by pressure distortion over the curved interface and flow reversal in the secondary expansion process of bubbles.

Comparing the bubble and the free surface motion under different Reynolds numbers in Fig.4, the dimensionless times for the bubble to expand to the maximum radius for the three Reynolds numbers in Fig.4(a)

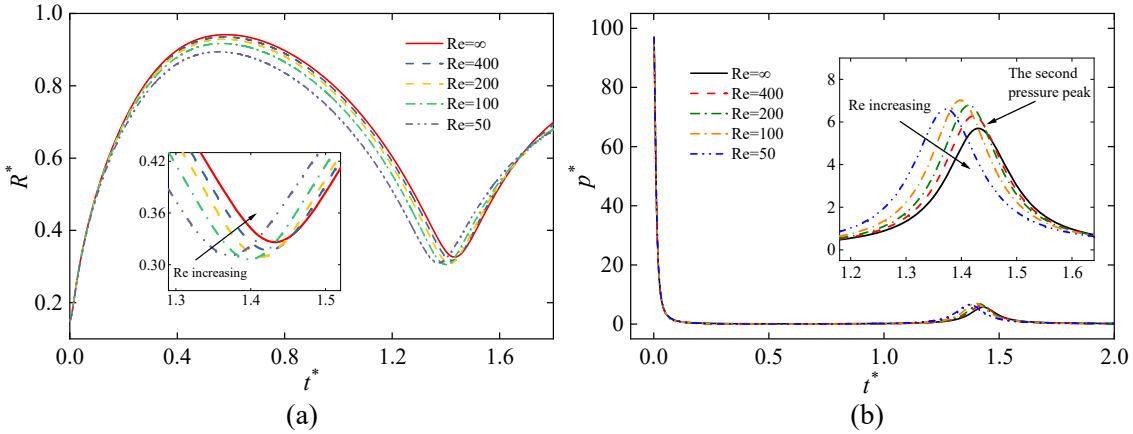

FIG. 5. Time histories of (a)equivalent radius of bubbles ;(b)average pressure in bubbles with different Reynolds numbers Re = 50, 100, 200, 400, ∞, and stand-off parameter $\gamma_d = 0.5$, respectively.

are $t^* = 0.581$, 0.576 and 0.566, respectively. Due to the hindrance of the liquid viscosity, the bubble expands to the maximum radius earlier when Re = 50. Moreover, the high-pressure region also decreases with the Reynolds number decrease. The main reason is that the liquid velocity flowing to this area on both sides of the bubble is slowed down by viscous retardation, and the impact effect is weakened. When the viscous effect is considered, the bubble jet velocity also changes. From the contours in Fig.4(b), the jet velocity decreases with the Reynolds number, and the shape of the top of the bubble jet is also smoother at small Re. The viscous friction is related to the velocity gradient, so the kinetic energy dissipates rapidly near the jet region, which leads to a smaller jet velocity when Re = 50. Because of the reduced velocity, the impact pressure formed by the small Re bubble jet penetrating the bottom is smaller than that in the inviscid case. The different bubble shapes differed significantly when the bubbles shrunk to the minimum volume. The bubble with Re = 50 has almost no toroidal bubble splitting (generated by an annular "sideways jet"), as shown in Fig.4(c). It is noteworthy that the ambient pressure increases with the decrease of the Reynolds number, mainly because viscous dissipation transforms liquid kinetic energy into internal energy, thus causing pressure increase. Due to the obstruction of viscosity, the crown height caused by the second cycle pulsation of low Reynolds number bubbles is much smaller than that under the inviscid condition in Fig.4(d).

Significant differences exist in the maximum bubble radius and period at different Reynolds numbers. Fig.5(a) shows the evolution of the equivalent radius of the bubble pulsation with time. During the first quarter of the pulsation period, the initial internal pressure pushes the bubble to expand rapidly, resulting in a large instantaneous Reynolds number. At this time, due to the small velocity gradient, the effect of liquid viscosity is relatively weak, and there is no noticeable difference in the radius of bubbles with different Reynolds numbers. It is necessary to know that the viscous force always exists and continuously accumulates in the bubble. As the Reynolds number decreased, the maximum equivalent radius of the bubble decreased, and the period also decreased. After the internal bubble pressure is less than the liquid field, it continues to expand under inertia, and the viscosity dissipates the kinetic energy so that the bubble cannot reach a larger radius. Unlike BEM or BIM, the pressure inside the bubble calculated by the EFEM model is not evenly distributed. Since the unevenly distributed pressure is difficult to be compared, the average pressure variation of the gas inside the bubble is calculated in this paper, as shown in Fig.5(b). It can be found that during most of the first period of bubble pulsation, the average pressure in the bubble has little difference under different Reynolds number conditions. Comparing the second pressure peak (corresponding to the minimum volume of the bubble), as shown in Fig.5(b), the average pressure peak shows a non-monotonic variation as the Reynolds number decreases, with the peak first increasing and then decreasing. However, it is worth noting that this law does not apply to the stand-off parameter $\gamma_d = 1.0$, 1.2, and 1.5. In these cases, the average pressure peak in the bubble decreases with the decrease of the Reynolds number. At the same time, the minimum equivalent radius increases with decreasing Reynolds number, which is caused by the strength of the bubble-free surface interaction.

Fig.6(a) shows the position of the top and bottom of the bubble at the axis. As the air above the free surface always maintains atmospheric pressure, the liquid pressure around the top of the bubble is less than the bottom when the bubble expands, leading to a faster expansion speed of the top, showing the phenomenon that the free surface attracts the bubble. When the bubble begins to collapse, the top is more

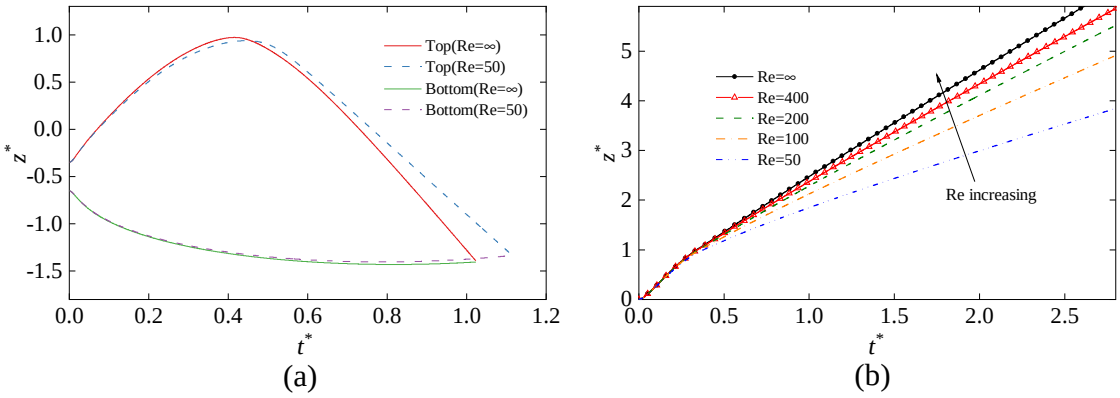

FIG. 6. Time histories of (a)the bubble top and bottom locations at Re $= \infty$ and 50, $\gamma_d = 0.5$; (b)the free surface spike height at different Reynolds numbers Re $= 50, 100, 200, 400, \infty$, and stand-off parameter $\gamma_d = 0.5$, respectively.

violently affected by the high-pressure region than the bottom. The jet penetrates the bottom at about $t^* = 1.03$, while the Re $= 50$ bubble jet penetrates at $t^* = 1.13$. The slope of the displacement curve of the bubble in Fig.6(a) represents the jet velocity. It can be found that compared with the bubble with Re $= 50$, the jet velocity is faster without considering the viscosity of the liquid. Meanwhile, compared with Fig.4(a), it can also be found that the inviscid bubble has formed an obvious top jet before the bubble reaches the maximum volume.

The evolution of the free surface spike height at different Reynolds numbers is shown in Fig.6(b). In the initial expansion stage of the bubble, due to the relatively long distance from the free surface, the change of the free surface with different Re is the same. It can be seen from Fig.6(b) that as the Re decreases, the viscous effect increases and the height of the jet on the free surface decreases significantly. The main reason is the significant rate of change of tangential velocity caused by the jet, which leads to sizeable viscous friction and faster kinetic energy loss.

The pulsation of the bubble in the second period induces a low axisymmetric water skirt on both sides of the free-surface jet, called the crown spike. Fig.7(a) shows the shape of the crown spike under different Reynolds numbers Re when the bubble expands to the maximum volume in the second pulsation cycle. With the increase in Reynolds number, the phenomenon of a crown spike is more pronounced, and the height of the water skirt is also increasing. And the shape is sharp, and when Re $= 50$, the free surface almost does not form a crown spike, indicating that the viscous effect weakens the evolution of the free surface. Fig.7(b) shows the shapes of bubbles when jet impact with different Reynolds numbers. The Re $= \infty$ bubble jet has a bulge at the front, called a mushroom-shaped jet. Koukouvinis[26] believes that the jet is caused by interface instability. However, compared with an inviscid bubble, the jet tip at the top of low Reynolds number bubbles is smoother, and no mushroom-shaped jet appears. Meanwhile, the volume of jet penetration is smaller, and the velocity and impact strength of the bubble jet is weak, which is reflected in the contours in Fig.4.

The bubble expands under the initial pressure. With the increase of liquid viscosity, the Reynolds number under the corresponding conditions decreases. The retardation effect of viscosity on bubble expansion becomes stronger and stronger, and the maximum radius of the bubble decreases. At the same time, the bubble jet is also affected by the viscosity, the jet velocity decreases with the decrease of the Reynolds number, and the jet penetration time is also delayed. The viscosity of the liquid affects the height and speed of the free surface jet: the viscosity increases, and the speed and height of the free surface jet decrease. When the viscosity increases to a specific value, the free surface crown spike generated by the pulsation of the bubbles will disappear, and the viscosity of the liquid weakens the interaction between bubbles and the free surface.

B. Bubble dynamics with different stand-off parameters

In the same fluid, the viscosity coefficient of the liquid has been determined. When a pulsating bubble is generated using the same method, the effect of viscosity on bubbles is unchanged. The parameter that affects the dynamics of bubbles and the free surface is the distance d (as shown in Fig.1(a)), and the dimensionless parameter γ_d represents the inception depth of the bubble. Set Re $= 100$, other parameters remain the same

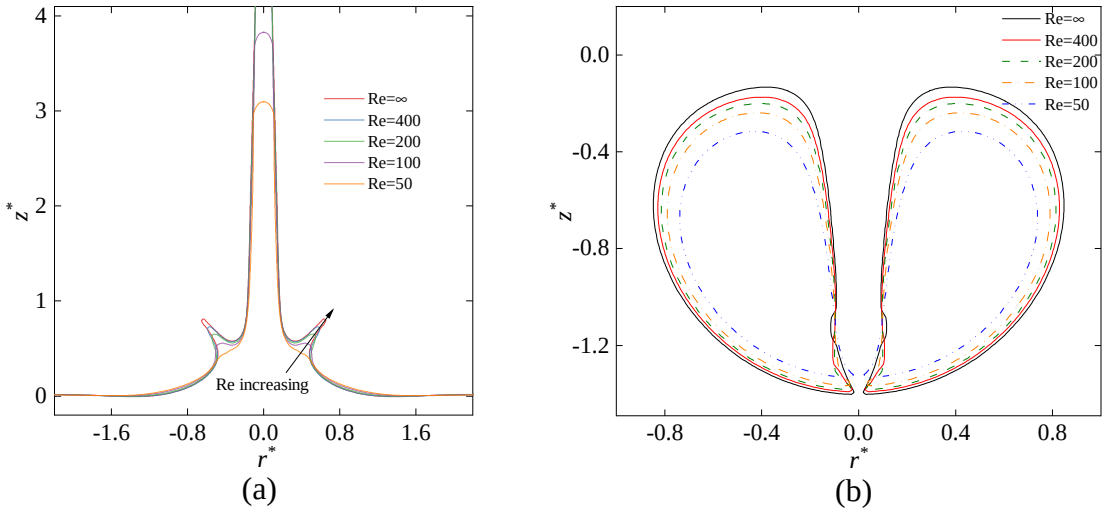

FIG. 7. (a)Shape of the free surface; (b)shape of the bubble when the jet impact at different Reynolds numbers $\mathrm{Re} = 50, 100, 200, 400, \infty$, and stand-off parameter $\gamma_d = 0.5$, respectively.

as the previous section, and study the bubble dynamics for $\gamma_d = 0.5 - 1.5$.

Fig.8 shows the bubble and the free surface shapes, pressure, and velocity contours at three important moments when Reynolds number $\mathrm{Re} = 100$ and stand-off parameter $\gamma_d = 0.5$, 1.0 and 1.5, respectively, corresponding to maximum bubble volume, jet impact, and maximum volume in the second pulsation period. The dimensionless time for the bubble to expand to the maximum radius increases with γ_d, $t^* = 0.576$, 0.775, and 0.848, respectively, as shown in Fig.8. The bubble jet is already formed in the expansion phase when $\gamma_d = 0.5$, while the bubble jet in the other two cases starts to form in the contraction phase. Compared with the other two conditions, the bubble and the free surface jet with smaller γ_d are also more slender, and the jet impacts the bottom earlier. As shown in Fig.8(b), bubble jets of $\gamma_d = 1.0$ and 1.5 impacting the bottom occurred near the moment when bubbles collapsed to the minimum volume. In contrast, bubble jets of $\gamma_d = 0.5$ had penetrated through the bottom in the contraction stage, and a local high-pressure region was formed when the jets penetrated through the bottom. It can be seen from Fig.8(c) that the bubble with $\gamma_d = 0.5$ produces toroidal splitting because the jet penetrates the bottom earlier, and the annular sideways jet is generated when the bubble continues to collapse. This phenomenon is noticeable at large Reynolds numbers, and bubbles with larger stand-off parameters do not produce apparent toroidal splitting. At the same time, with the increase of γ_d, the free surface jet becomes lower, and the phenomenon of a crown spike is less obvious. The free surface does not produce a crown spike during the secondary pulsation of the bubble when $\gamma_d = 1.5$.

Fig.9(a) shows the shape of the bubble when the jet penetrates with different γ_d. It can be seen from the figure that with the increase of the stand-off parameter, the volume of bubble jet impact continues to decrease. When the inception depth is small, the impact time of the jet is earlier than the minimum volume time due to the strong interaction between bubbles and the free surface. The bubble jet width also varies with the change of the stand-off parameter. When the γ_d increases from 0.5 to 1.0, the jet width gradually increases; when the γ_d increases from 1.0 to 1.5, the jet width gradually decreases, which is the same as the law obtained by Li[38] without considering viscosity. With the increase of γ_d, the water jet penetration time is delayed, and the jet width changes due to the different degrees of bubble shrinkage. It can also be seen from the velocity contours in Fig.8(b) that the velocity of the jet impinges increases with the increase of γ_d. Fig.9(b) shows the shape of the free surface when the jet penetrates. With the increase of γ_d, the jet height of the free surface decreases while the jet width gradually increases. From the pressure contours in Fig.8(a), there is no high-pressure region below the free surface when the γ_d is large, which is not conducive to the generation of the bubble and the free surface jet. At the same time, the effect of bubble expansion on the free surface is weakened, which is also the reason for the low height of the free surface jet. Fig.10 shows the position changes of the top and bottom of the bubble on the axis, which can vividly see the changing trend of the axial length of the bubble. Meanwhile, the velocity of the bubble surface at the axis can also be obtained by calculating the slope of the curve. In the early stage of bubble expansion, the displacement of the upper surface of bubbles with different γ_d is different, and the displacement decreases with the increase

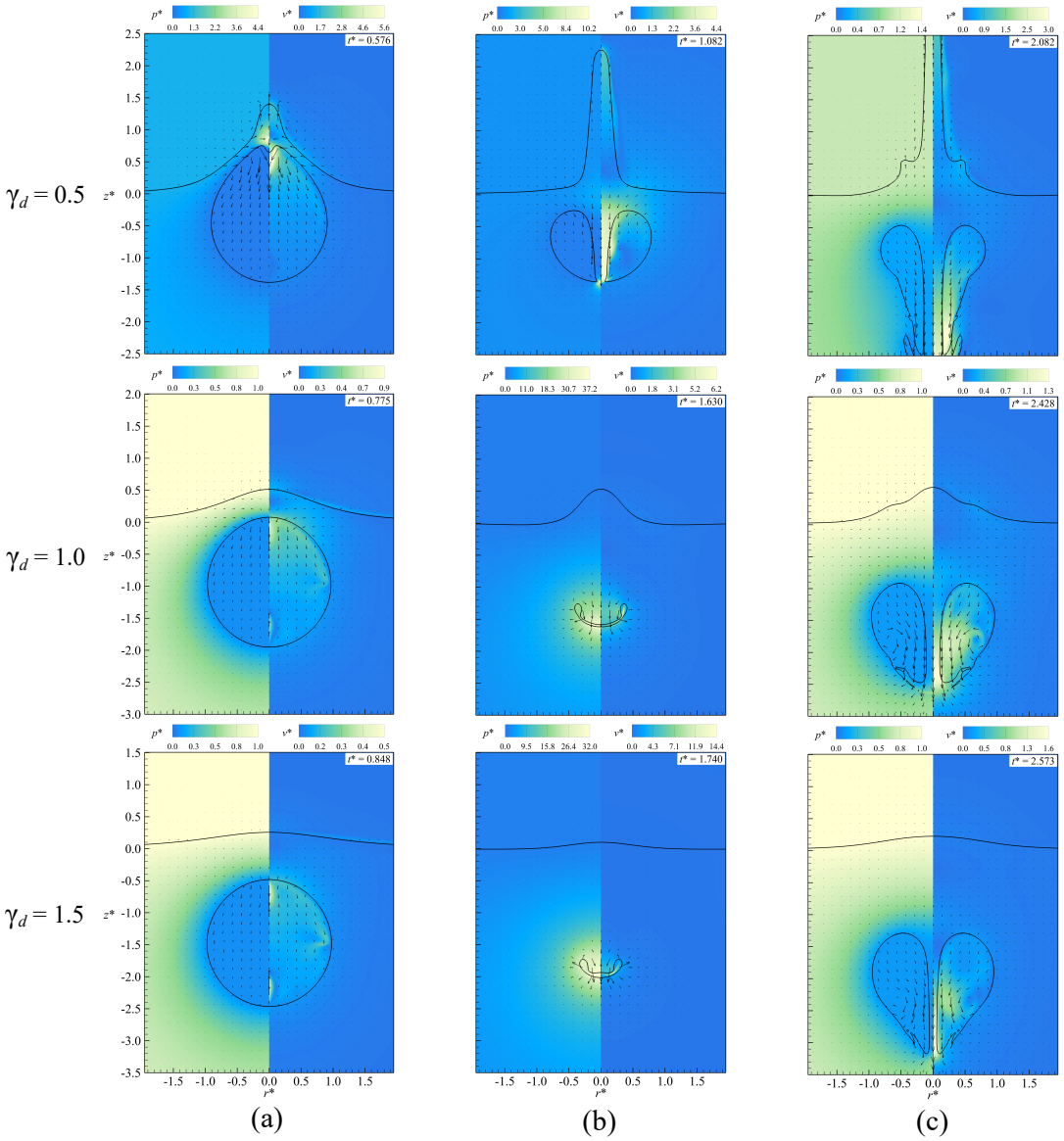

FIG. 8. Pressure and velocity contours at $\gamma_d = 0.5, 1.0, 1.5$, Re=100, respectively:(a) maximum volume; (b) jet impact; (c) bubble second pulsation period. The black line represents the bubble boundary and the free surface boundary; the left colored contour represents the pressure field; the arrow and the right colored contour represent the velocity field.

of γ_d. However, the displacement of the lower surface changes almost the same, mainly because the existence of the free surface affects the movement of the upper surface of bubbles. It is worth noting that at $\gamma_d = 1.5$, the axial bubble jet does not directly penetrate the bottom, but generates a temporary air cushion, as shown in Fig.8(b) and Fig.9(a). This is mainly because the bubble jet at impact is very wide and penetrates the side walls of the bubble first rather than the bottom. According to the slope analysis of the bubble top displacement curve in Fig.11(a), it can be found that the jet with $\gamma_d = 1.5$ is always in the acceleration stage from bubble contraction to jet slamming, which is the reason why the bubble jet velocity increases with the increase of γ_d.

The time histories curve of the equivalent radius of bubble pulsation with different stand-off parameters γ_d is shown in Fig.11(a). With the increase of the bubble-free surface distance, the maximum equivalent radius of the bubble increases, the minimum equivalent radius decreases, and the influence of the free surface on the bubble gradually decrease. The diamonds in Fig.11(a) represent the moment when the liquid jet penetrates the bubbles' bottom. With the decrease of the stand-off parameter, the time of jet penetration is advanced.

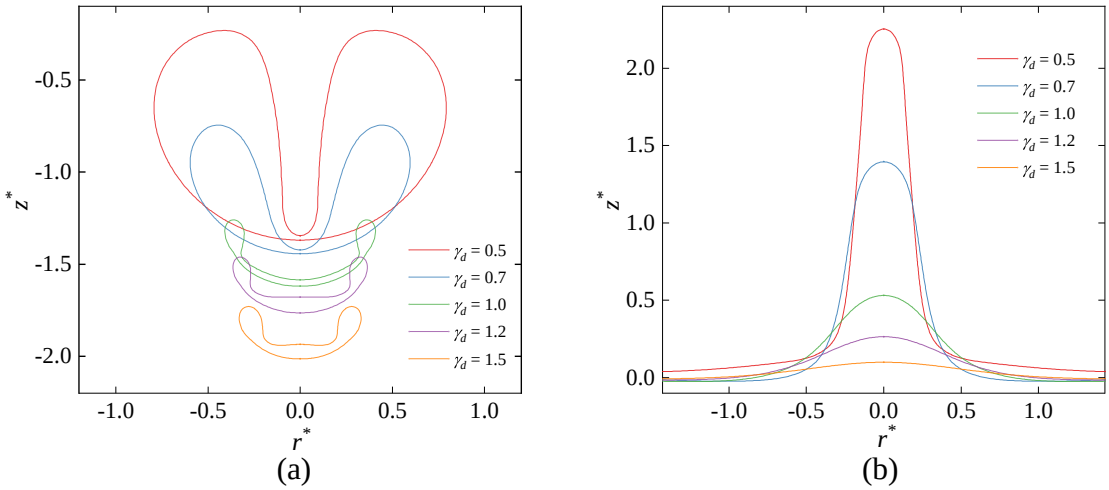

FIG. 9. The shape of (a)the bubble; and (b)the free surface before the jet penetrates the bottom at γ_d=0.5, 0.7, 1.0, 1.2, and 1.5, Re=100, respectively.

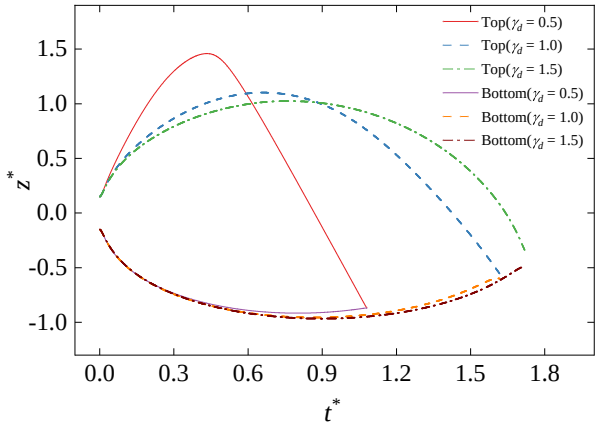

FIG. 10. Time histories of the bubble top and bottom locations at γ_d=0.5,1.0,1.5, Re=100, respectively.

For $\gamma_d = 0.5$ and 0.7, the jet penetration occurs in the contraction phase of the first pulsation period. In contrast, the bubble jet penetration for $\gamma_d = 1.0$, 1.2, and 1.5 occurs in the second pulsation period. Because the buoyancy parameter δ is relatively small, the primary influence on the jet is the free surface. In the case with a greater stand-off distance, the repulsion effect of the free surface on the bubble is weaker and a delay in the jet penetration is observed.

Fig.11(b) shows the variation of the average pressure in the bubble with time. The average internal pressure of bubbles with different γ_d has little difference in the first pulsation cycle and is at a small value most of the time. The second pressure peak (corresponding to the bubble's collapse to the minimum volume) increases with increasing γ_d, and the bubble radius at the time corresponding to the peak pressure decreases with increasing γ_d. Because bubbles with small distance parameters do more work on the free surface and lose more energy, thus resulting in smaller internal pressure of bubbles.

IV. CONCLUSIONS

A dynamic model is established for the interaction between a bubble and a free surface in a viscous compressible liquid based on the EFEM coupled with the VOF. The numerical model is verified by the spherical bubble theories and experiments with excellent agreement. Bubble dynamics and free surface evolution are analyzed in terms of the Reynolds number Re and the dimensionless inception depth γ_d of the bubble. The following features are observed:

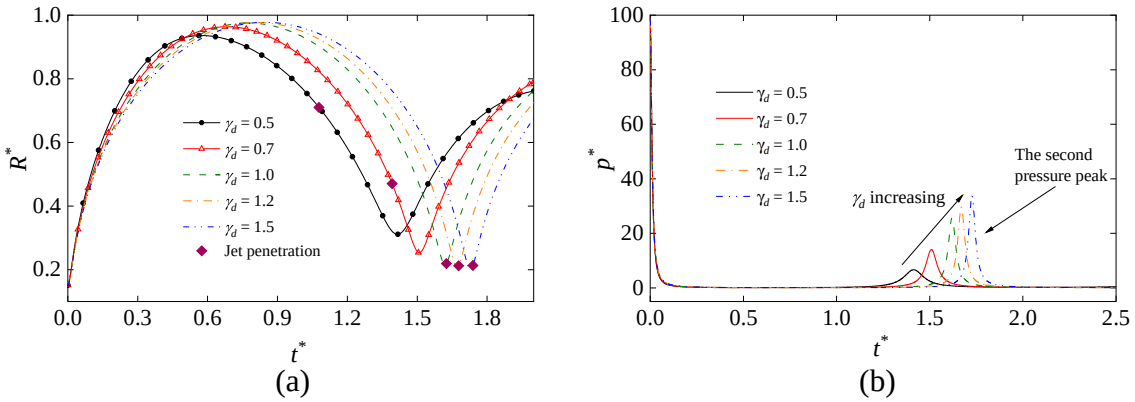

FIG. 11. Time histories of (a)the equivalent radius of bubbles; (b)average pressure in bubbles with different stand-off parameters γ_d=0.5, 0.7, 1.0, 1.2, and 1.5, Re=100, respectively.

(I) As Re decreases, the bubble oscillation amplitude and period decrease, the bubble jet shape is blunter, the jet velocity decrease, and the impact time is delayed. At a lower Re, the jet is weaker and associated with less kinetic energy, resulting in earlier collapse. The viscosity also reduces the toroidal bubble splitting during pulsation, and the bubble with Re=50 hardly splits.

(II) As γ_d increases, the maximum bubble volume increases, the minimum bubble volume decreases, and the second pressure peak of the bubble increases. When γ_d decreases from 1.5 to 0.5, the jet becomes sharper and impacts the opposite bubble surface earlier.

(III) As Re decreases, the height and velocity of the free surface jet decrease, and the crown spike height decreases or even disappears in the second pulsation cycle. As γ_d increases, the free surface jet's height decreases, the jet's width increases, and the crown spike tends to be low or even disappear.

ACKNOWLEDGMENTS

The authors would like to acknowledge support from the Finance Science and Technology Project of Hainan Province (Grant No. ZDKJ2021020), the National Natural Science Foundation of China (Grant Nos. 52088102 and 51909041), the Natural Science Foundation of Heilongjiang Province of China(No. YQ2021E012) and Development Program(JCKY2021604B027). Thanks to Dr. Hao Tang for his help in the data analysis of this paper.

[1]A. M. Zhang, W. B. Wu, Y. L. Liu, and Q. X. Wang, "Nonlinear interaction between underwater explosion bubble and structure based on fully coupled model," Physics of Fluids **29**, 082111 (2017).
[2]E. Klaseboer, K. C. Hung, C. Wang, C. W. Wang, B. C. Khoo, P. Boyce, S. Debono, and H. Charlier, "Experimental and numerical investigation of the dynamics of an underwater explosion bubble near a resilient/rigid structure," Journal of Fluid Mechanics **537**, 387–413 (2005).
[3]X. L. Yao, A. M. Zhang, and Y. C. Liu, "Interaction of two three-dimensional explosion bubbles," Journal of Marine Science and Application **6**, 7 (2007).
[4]A. M. Zhang and Y. L. Liu, "Improved three-dimensional bubble dynamics model based on boundary element method," Journal of Computational Physics **294**, 208–223 (2015).
[5]A. Tatlısuluoğlu and S. Beji, "Blast pressure measurements of an underwater detonation in the sea," Journal of Marine Science and Application , 1–8 (2021).
[6]N. Zhang, Z. Zong, and W. P. Zhang, "Dynamic response of a surface ship structure subjected to an underwater explosion bubble," Marine Structures **35**, 26–44 (2014).
[7]G. Li, D. Shi, L. Wang, and K. Zhao, "Measurement technology of underwater explosion load: A review," Ocean Engineering **254**, 111383 (2022).
[8]S. S. Emamzadeh, "Nonlinear dynamic response of a fixed offshore platform subjected to underwater explosion at different distances," Journal of Marine Science and Application **21**, 168–176 (2022).
[9]Q. X. Wang and K. Manmi, "Three dimensional microbubble dynamics near a wall subject to high intensity ultrasound," Physics of Fluids **26**, 032104 (2014).
[10]H. Lais, P. S. Lowe, T. H. Gan, and L. C. Wrobel, "Numerical modelling of acoustic pressure fields to optimize the ultrasonic cleaning technique for cylinders," Ultrasonics Sonochemistry **45**, 7–16 (2018).
[11]W. D. Song, M. H. Hong, B. Lukyanchuk, and T. C. Chong, "Laser-induced cavitation bubbles for cleaning of solid surfaces," Journal of Applied Physics **95**, 2952–2956 (2004).

[12]D. S. Fatyukhin, R. I. Nigmetzyanov, V. M. Prikhodko, A. V. Sukhov, and S. K. Sundukov, "A comparison of the effects of ultrasonic cavitation on the surfaces of 45 and 40kh steels," Metals **12**, 138 (2022).
[13]J. Mustonen, O. Tommiska, A. Holmström, T. Rauhala, P. Moilanen, M. Gritsevich, A. Salmi, and E. Hæggström, "Fem-based time-reversal enhanced ultrasonic cleaning," Ultrasonics Sonochemistry **79**, 105798 (2021).
[14]E. Stride and N. S. Ari, "Microbubble ultrasound contrast agents: a review," Proceedings of the Institution of Mechanical Engineers Part H Journal of Engineering in Medicine **217**, 429–47 (2003).
[15]P. G. Durham and P. A. Dayton, "Applications of sub-micron low-boiling point phase change contrast agents for ultrasound imaging and therapy," Current Opinion in Colloid & Interface Science **56**, 101498 (2021).
[16]H. Yusefi and B. Helfield, "Ultrasound contrast imaging: Fundamentals and emerging technology," Frontiers in Physics , 100 (2022).
[17]C. B. Arnold, P. Serra, and A. Piqué, "Laser direct-write techniques for printing of complex materials," Mrs Bulletin **32**, 23–31 (2007).
[18]M. Jalaal, M. K. Schaarsberg, C.-W. Visser, and D. Lohse, "Laser-induced forward transfer of viscoplastic fluids," Journal of fluid mechanics **880**, 497–513 (2019).
[19]P. Serra and A. Piqué, "Laser-induced forward transfer: fundamentals and applications," Advanced Materials Technologies **4**, 1800099 (2019).
[20]R. N. Cui, S. Li, S. P. Wang, and A. M. Zhang, "Pulsating bubbles dynamics near a concave surface," Ocean Engineering **250**, 110989 (2022).
[21]Q. X. Wang, "Non-spherical bubble dynamics of underwater explosions in a compressible fluid," Physics of Fluids **25**, 072104 (2013).
[22]A. M. Zhang, P. Cui, J. Cui, and Q. X. Wang, "Experimental study on bubble dynamics subject to buoyancy," Journal of Fluid Mechanics **776**, 137–160 (2015).
[23]P. Koukouvinis, M. Gavaises, O. Supponen, and M. Farhat, "Numerical simulation of a collapsing bubble subject to gravity," Physics of Fluids **28**, 032110 (2016).
[24]S. Li, B. C. Khoo, A. M. Zhang, and S. P. Wang, "Bubble-sphere interaction beneath a free surface," Ocean Engineering **169**, 469–483 (2018).
[25]L. T. Liu, X. L. Yao, A. M. Zhang, and Y. Y. Chen, "Numerical analysis of the jet stage of bubble near a solid wall using a front tracking method," Physics of Fluids **29**, 012105 (2017).
[26]P. Koukouvinis, M. Gavaises, O. Supponen, and M. Farhat, "Simulation of bubble expansion and collapse in the vicinity of a free surface," Physics of Fluids **28**, 052103 (2016).
[27]A.-M. Zhang, S.-M. Li, P. Cui, S. Li, and Y.-L. Liu, "Interactions between a central bubble and a surrounding bubble cluster," Theoretical and Applied Mechanics Letters , 100438 (2023).
[28]L. Liu, J. Wang, and K. Tang, "Coupling characteristics of bubbles with a free surface initially disturbed by water waves," Physics of Fluids **34**, 042117 (2022).
[29]A. Pearson, E. Cox, J. R. Blake, and S. R. Otto, "Bubble interactions near a free surface," Engineering Analysis with Boundary Elements **28**, 295–313 (2004).
[30]Q. Wang, K. Yeo, B. Khoo, and K. Lam, "Nonlinear interaction between gas bubble and free surface," Computers & fluids **25**, 607–628 (1996).
[31]Y. L. Liu, Q. X. Wang, S. P. Wang, and A. M. Zhang, "The motion of a 3d toroidal bubble and its interaction with a free surface near an inclined boundary," Physics of Fluids **28**, 122101 (2016).
[32]Y. Sun, Z. Yao, H. Wen, Q. Zhong, and F. Wang, "Cavitation bubble collapse in a vicinity of a rigid wall with a gas entrapping hole," Physics of Fluids **34**, 073314 (2022).
[33]J. R. Blake and D. C. Gibson, "Growth and collapse of a vapour cavity near a free surface," J. Fluid Mech. **111**, 123–123 (1981).
[34]J. R. Blake and D. C. Gibson, "Cavitation bubbles near boundaries," Annual Review of Fluid Mechanics **19**, 99–123 (1987).
[35]J. Li and J. L. Rong, "Bubble and free surface dynamics in shallow underwater explosion," Ocean Engineering **38**, 1861–1868 (2011).
[36]O. Supponen, D. Obreschkow, M. Tinguely, P. Kobel, N. Dorsaz, and M. Farhat, "Scaling laws for jets of single cavitation bubbles," Journal of Fluid Mechanics **802**, 263–293 (2016).
[37]S. Zhang, S. Wang, and A. Zhang, "Experimental study on the interaction between bubble and free surface using a high-voltage spark generator," Physics of Fluids **28**, 032109 (2016).
[38]T. Li, A. M. Zhang, S. P. Wang, S. Li, and W. T. Liu, "Bubble interactions and bursting behaviors near a free surface," Physics of Fluids **31**, 042104 (2019).
[39]L. T. Liu, X. B. Chen, W. Q. Zhang, and A. M. Zhang, "Study on the transient characteristics of pulsation bubble near a free surface based on finite volume method and front tracking method," Physics of Fluids **32**, 052107 (2020).
[40]Y. Saade, M. Jalaal, A. Prosperetti, and D. Lohse, "Crown formation from a cavitating bubble close to a free surface," Journal of Fluid Mechanics **926** (2021).
[41]N. Bempedelis, J. Zhou, M. Andersson, and Y. Ventikos, "Numerical and experimental investigation into the dynamics of a bubble-free-surface system," Physical Review Fluids **6**, 013606 (2021).
[42]R. T. Cerbus, H. Chraibi, M. Tondusson, S. Petit, D. Soto, R. Devillard, J. P. Delville, and H. Kellay, "Experimental and numerical study of laser-induced secondary jetting," Journal of Fluid Mechanics **934** (2022).
[43]T.-H. Phan, V.-T. Nguyen, and W.-G. Park, "Numerical study on strong nonlinear interactions between spark-generated underwater explosion bubbles and a free surface," International Journal of Heat and Mass Transfer **163**, 120506 (2020).
[44]S.-M. Li, A.-M. Zhang, and N.-N. Liu, "Effect of a rigid structure on the dynamics of a bubble beneath the free surface," Theoretical and Applied Mechanics Letters **11**, 100311 (2021).
[45]D. Singh and A. K. Das, "Dynamics of inner gas during the bursting of a bubble at the free surface," Physics of Fluids **33** (2021), 052105.
[46]Q. Wang, W. Liu, C. Corbett, and W. R. Smith, "Microbubble dynamics in a viscous compressible liquid subject to ultrasound," Physics of fluids , 34 (2022).

[47]Z. Wang, R. Duan, L. Liu, and H. Yang, "Jetting behavior as a bubble bursts in free space," Physics of Fluids **33**, 023304 (2021).
[48]M. S. Plesset, "The dynamics of cavitation bubbles," J.appl.mech **16**, 277–282 (1949).
[49]J. B. Keller and M. Miksis, "Bubble oscillations of large amplitude," The Journal of the Acoustical Society of America **68**, 628–633 (1980).
[50]A.-M. Zhang, S.-M. Li, P. Cui, S. Li, and Y.-L. Liu, "A unified theory for bubble dynamics," Physics of Fluids **35**, 033323 (2023).
[51]Q. Wang, K. Yeo, B. Khoo, and K. Lam, "Strong interaction between a buoyancy bubble and a free surface," Theoretical and Computational Fluid Dynamics **8**, 73–88 (1996).
[52]A. M. Zhang and B. Y. Ni, "Three-dimensional boundary integral simulations of motion and deformation of bubbles with viscous effects," Computers & Fluids **92**, 22–33 (2014).
[53]S. J. Lind and T. N. Phillips, "The effect of viscoelasticity on the dynamics of gas bubbles near free surfaces," Physics of Fluids **25**, 022104 (2013).
[54]S. Li and B. Y. Ni, "Simulation on the interaction between multiple bubbles and free surface with viscous effects," Engineering Analysis with Boundary Elements **68**, 63–74 (2016).
[55]B. Y. Ni, A. M. Zhang, and G. X. Wu, "Simulation of a fully submerged bubble bursting through a free surface," European Journal of Mechanics - B/Fluids **55**, 1–14 (2016).
[56]M. J. Miksis, J. M. Vanden Broeck, and J. B. Keller, "Rising bubbles," Journal of Fluid Mechanics **123**, 31–41 (1982).
[57]T. Lundgren and N. Mansour, "Oscillations of drops in zero gravity with weak viscous effects," Journal of Fluid Mechanics **194**, 479–510 (1988).
[58]J. M. Boulton-Stone, "The effect of surfactant on bursting gas bubbles," Journal of Fluid Mechanics **302**, 231–257 (1995).
[59]S. Popinet and S. Zaleski, "Bubble collapse near a solid boundary: a numerical study of the influence of viscosity," Journal of Fluid Mechanics **464**, 137–163 (2002).
[60]Y. L. Liu, A. M. Zhang, Z. L. Tian, and S. P. Wang, "Investigation of free-field underwater explosion with eulerian finite element method," Ocean Engineering **166**, 182–190 (2018).
[61]L. T. Liu, X. L. Yao, N. N. Liu, and F. L. Yu, "Toroidal bubble dynamics near a solid wall at different reynolds number," International Journal of Multiphase Flow **100**, 104–118 (2018).
[62]Y. L. Liu, A. M. Zhang, Z. L. Tian, and S. P. Wang, "Dynamical behavior of an oscillating bubble initially between two liquids," Physics of Fluids **31**, 092111 (2019).
[63]S. Li, Y. Saade, D. van der Meer, and D. Lohse, "Comparison of boundary integral and volume-of-fluid methods for compressible bubble dynamics," International Journal of Multiphase Flow **145**, 103834 (2021).
[64]O. Supponen, D. Obreschkow, P. Kobel, and M. Farhat, "Detailed jet dynamics in a collapsing bubble," Journal of Physics: Conference Series **656**, 012038 (2015).
[65]M. Ivings, D. Causon, and E. Toro, "On riemann solvers for compressible liquids," International Journal for Numerical Methods in Fluids **28**, 395–418 (1998).
[66]Z. L. Tian, Y. L. Liu, A. M. Zhang, and S. P. Wang, "Analysis of breaking and re-closure of a bubble near a free surface based on the eulerian finite element method," Computers & Fluids **170**, 41–52 (2018).
[67]H. Tang, Y. L. Liu, P. Cui, and A. M. Zhang, "Numerical study on the bubble dynamics in a broken confined domain," Journal of Hydrodynamics **32**, 1029–1042 (2020).
[68]Z. L. Tian, Y. L. Liu, A. M. Zhang, L. B. Tao, and L. Chen, "Jet development and impact load of underwater explosion bubble on solid wall," Applied Ocean Research **95**, 102013 (2020).
[69]H. Tang, Z.-L. Tian, X.-Y. Ju, J.-T. Feng, Y.-L. Liu, and A.-M. Zhang, "Experimental and numerical investigations on the explosions nearby a free surface from both sides," Ocean Engineering **278**, 114372 (2023).
[70]D. J. Benson and S. Okazawa, "Contact in a multi-material eulerian finite element formulation," Computer Methods in Applied Mechanics and Engineering **193**, 4277–4298 (2004).
[71]W. T. Liu, A. M. Zhang, X. H. Miao, F. R. Ming, and Y. L. Liu, "Investigation of hydrodynamics of water impact and tail slamming of high-speed water entry with a novel immersed boundary method," Journal of Fluid Mechanics **958**, A42 (2023).
[72]Z. L. Tian, Y. L. Liu, A. M. Zhang, and L. B. Tao, "Energy dissipation of pulsating bubbles in compressible fluids using the eulerian finite-element method," Ocean Engineering **196**, 106714 (2020).
[73]D. J. Benson, "Computational methods in lagrangian and eulerian hydrocodes," Computer Methods in Applied Mechanics and Engineering **99**, 235–394 (1992).
[74]R. Han, A. M. Zhang, S. Tan, and S. Li, "Interaction of cavitation bubbles with the interface of two immiscible fluids on multiple time scales," Journal of Fluid Mechanics **932** (2022).